# UC Berkeley

## UC Berkeley Previously Published Works


### Title

Extended Cycling through Rigid Block Copolymer Electrolytes Enabled by Reducing Impurities in Lithium Metal Electrodes


### Permalink

https://escholarship.org/uc/item/3425m6hz



### Journal

ACS Applied Energy Materials, 2(11)

### ISSN

2574-0962



### Authors

Maslyn, Jacqueline A
Frenck, Louise
Loo, Whitney S
et al.



### Publication Date

2019-11-25

### DOI

10.1021/acsaem.9b01685

Peer reviewed



eScholarship.org Powered by the California Digital Library
University of California

# Extended Cycling through Rigid Block Copolymer Electrolytes Enabled by Reducing Impurities in Lithium Metal Electrodes

Jacqueline A. Maslyn [a, b], Louise Frenck [a], Whitney S. Loo [a], Dilworth Y. Parkinson [c], Nitash P. Balsara [a, b, d, *]

[a] Department of Chemical and Biomolecular Engineering, University of California, Berkeley, California 94720, USA

[b] Materials Sciences Division, Lawrence Berkeley National Laboratory, Berkeley, California, 94720, USA

[c] Advanced Light Source, Lawrence Berkeley National Laboratory, Berkeley, California 94720, USA

[d] Energy Technologies Area, Lawrence Berkeley National Laboratory, Berkeley, California 94720, USA

* Corresponding author. E-mail: nbalsara@berkeley.edu, Phone: 1-510-642-8973.

## ABSTRACT

Successful prevention of lithium dendrite growth would enable the use of lithium metal as an anode material in next-generation rechargeable batteries. Mechanically stiff block copolymer electrolytes have been shown to prolong the life of lithium metal cells by suppressing lithium dendrite growth. However, impurity particles that are invariably present in the lithium metal nucleate electrodeposition defects that eventually lead to short-circuits. In this study, we use X-ray tomography to study the morphology of electrodeposited lithium in symmetric cells containing a block copolymer electrolyte. An “electrochemical filtering” treatment was performed on these cells in order to reduce the concentration of impurity particles near the electrode-electrolyte interface, and cells were cycled to determine the effects of the treatment on lifetime. Depending on the treatment details, average charge passed before failure was improved by 30-400%. For a cell in which the treatment was most effective, cycle life was increased by more than an order of magnitude and the measured defect density was negligible. Other treated cells, however, in which the treated lithium was imperfect, had a higher areal density of defects compared to control cells. A majority of the defects in treated cells were confined within the electrodes. In contrast, most of the defects seen in the control cells were protrusions that invaded the electrolyte phase. The increased lifetime in these imperfectly treated cells was not due to a reduction in defect density, but rather due to the differences in defect morphology. These results motivate the development of deposition defect- and impurity-free lithium metal electrodes.

## INTRODUCTION

The theoretical energy density of batteries incorporating a lithium metal anode is significantly higher than that of current lithium-ion batteries. There are, however, significant problems that preclude the development of practical rechargeable batteries with these anodes. A major factor that limits the cycle life of cells containing metallic lithium is the morphology of electrodeposited lithium. Protruding lithium structures, often called “dendrites” after the branched morphology of lithium deposition observed in liquid electrolytes, can span the electrolyte and cause a short-circuit. Studies of the development of these structures are important to fundamentally understand the nature of lithium electrodeposition through different electrolytes. X-ray tomography is a powerful technique for determining the three-dimensional morphology of electrodeposited lithium through both liquid[1–4] and solid polymer[5–10] electrolytes.

Many strategies for extending the cycle life of cells containing a lithium metal electrode have been reported in the literature. They include increasing the mechanical strength of the electrolyte,[11–13] synthesizing tortuous electrolytes to distribute ion flux,[14] engineering interfacial layers,[15,16] and developing single-ion conducting electrolytes to eliminate salt concentration gradients[17]. The lithium metal anode has also been subjected to different treatments in order to increase cell performance. [18–24]

In this paper, we use a nanostructured polystyrene-*block*-poly(ethylene oxide) (SEO) block copolymer mixed with lithium bis(trifluoromethanesulfonyl)imide (LiTFSI). In this class of solid polymer electrolytes, planar, crystalline lithium deposition is observed over most of the cell area.[10] Nonplanar protrusions are only

observed in the vicinity of impurity particles present in commercially available lithium foils.[5] As the reported impurities in lithium metal are primarily oxygen and nitrogen, we hypothesize that the impurities are $Li_2O$, LiOH, and $Li_3N$. It is likely that impurity particles at the electrode-electrolyte interface cause inhomogeneities in the local current density and promote the nucleation of lithium protrusions. These particles do not pass through the electrolyte during electrodeposition.[8] Stable deposition of planar lithium without protrusions is obtained at low current densities (less than 0.08 mA $cm^{-2}$) in spite of impurity particles.[10]

Based on the work described in the previous paragraph, we hypothesized that electrodepositing lithium at a low current density (0.04 mA $cm^{-2}$) through an SEO/LiTFSI electrolyte in a lithium symmetric cell would lead to an impurity-free layer of lithium. We call this process “electrochemical filtering”. We show that the electrochemically filtered lithium layer is not perfect. Nevertheless, our approach enables a systematic study of the effect of reducing the concentration of impurity particles on lithium electrodeposition during cycling. We demonstrate that electrochemical filtering improves cycle life by more than an order of magnitude.

## EXPERIMENTAL SECTION

*Anionic synthesis and polymer purification.* The polystyrene-*block*-poly(ethylene oxide) (PS-PEO, or SEO) diblock copolymer was synthesized via sequential high-vacuum living anionic polymerization, using sec-butyllithium as the initiator for styrene polymerization and P4 tert-butylphosphazene base as the promoter for the polymerization of ethylene oxide.[25–27] SEO(115-172) was further purified as given in ref. [10], where the numbers in the parentheses correspond to the number-averaged molecular weights of the PS and PEO blocks, $M_{PS}$ and $M_{PEO}$, respectively. The relevant properties of the SEO copolymers used in this study are provided in Table 1, where $\phi_{EO}$ refers to the volume fraction of PEO. GPC was conducted on an Agilent 1260 Infinity Series fitted with Water Styragel HR 3 and 4 columns. The polydispersity index (PDI) was measured using a polystyrene standard. The self-assembled morphology of the block copolymers is expected to be lamellar based on the PEO volume fraction.

**Table 1:** Properties of SEO polymers used in this study: name, molecular weight of the PS block, molecular weight of the PEO block, volume fraction PEO of the neat polymer, and polydispersity index.

| **Name** | **$M_{PS}$ [kg mol$^{-1}$]** | **$M_{PEO}$ [kg mol$^{-1}$]** | **$\varphi_{EO}$** | **PDI** |
|---|---|---|---|---|
| SEO(115-172) | 115 | 172 | 0.59 | 1.10 |
| SEO(200-222) | 200 | 222 | 0.51 | 1.08 |

Methods for electrolyte preparation and electrochemical cell fabrication closely mimic those previously reported.[10] All electrolyte preparation was carried out in an argon glove box with less than 0.1 parts per million (ppm) $H_2O$ and less than 0.1

ppm $O_2$. All lithium cell assembly was carried out in an argon glove box with less than 2.3 ppm $H_2O$ and less than 0.1 ppm $O_2$.

*Li-SEO-Li symmetric cell assembly for cycling and tomographic imaging.* — Lithium metal foil was purchased from FMC Lithium at 99.9% purity. The foil thickness was 150 µm. All sample preparation was performed in a glove box filled with Argon gas. A 7/16-inch diameter metal punch was used to cut a polymer electrolyte disc from a previously cast electrolyte film. Three layers of lithium metal foil were stacked on top of a piece of nickel foil, and then pressed until flat and shiny inside pouch material with a pneumatic press (130 MPa). The lithium electrodes were made by using a 3/8-inch diameter punch to cut through the three layers of lithium foil and nickel foil backing. The two, 450 µm thick, lithium electrodes were used to sandwich the polymer electrolyte membrane. Two 0.25 mm thick stainless steel shims were placed above and beneath the cell to keep the cell flat. Aluminum current collector tabs were then affixed to the stainless steel shims and the sample was vacuum sealed in polypropylene-lined aluminum pouch material. Pouched cells were annealed for 12 hours at 120 °C before beginning conditioning cycles.

*Conditioning, treatment, and cycling*. Cells were galvanostatically cycled in an Associated Environmental Systems SD-402 oven using a Maccor Series 4000 Battery Tester. Cells were allowed to equilibrate at the temperature of interest (90 °C) for at least an hour before a current was imposed. Cells were occasionally paused during conditioning or polarization for practical reasons (e.g., while removing a failed cell). Each cell was subjected to fourteen conditioning cycles at 90 °C. During each cycle, a current density of 0.02 mA $cm^{-2}$ was imposed in one direction for 4 hours, followed by a 45 minute rest period, followed by the imposition of a constant current density of 0.02 mA $cm^{-2}$ in the opposite direction, followed by another 45 minute rest

period. The thickness of lithium transferred between the electrodes during each half cycle at 0.02 mA $cm^{-2}$ was 0.4 µm.

We report on results obtained from 23 separate cells. All of the cells were conditioned as described above and then subjected to further experiments as summarized in Table 2. Three different conditions were used for electrochemical filtering, labeled Treatments 1, 2, and 3 in Table 2. In the first electrochemical filtering step, lithium was deposited on to the lower electrode at a current density of 0.04 mA $cm^{-2}$. In the second, a portion of the electrodeposited lithium layer was deposited back on to the upper electrode at the same current density until the specified calculated thickness of lithium was reached. The thickness of the deposited lithium during the first step was varied from 8.5 to 66 µm. The thickness of the deposited lithium during the second step was varied from 1.7 to 19 µm. Greater volumes of lithium were passed during Treatments 2 and 3 in order to clearly ascertain the effect of electrochemical filtering by X-ray tomography before cycling. Four batches of cells were fabricated on four days: one batch each was used for Treatments 1-3 to minimize variations between cells, while the fourth batch was split between Treatments 1 and 3.

The efficacy of electrochemical filtering was studied in cycling experiments also summarized in Table 2. Treatment 1 cells were cycled at 0.12 mA $cm^{-2}$, corresponding to a cycled lithium layer thickness of 2.3 µm. Cells processed using Treatments 2 and 3 were cycled at 0.175 mA $cm^{-2}$, corresponding to a cycled lithium layer thickness of 3.4 µm. The current density used in Treatments 2 and 3 was higher to promote faster failure and shorten the experimental timescale. During each cycle, lithium was deposited on to the upper electrode for 4 hours, followed by a 45 minute rest period, followed by the imposition of a constant current density in

the opposite direction, followed by another 45 minute rest period. Cells were cycled until a sudden drop in the voltage required to maintain the target current density was observed. This was taken as the signature of a short-circuit caused by nonplanar lithium deposition. Treatment 2 was conducted with a different electrolyte in order to show that cycling improvements were not limited to a particular SEO electrolyte.

**Table 2.** Description of the three electrochemical filtering treatments applied to lithium symmetric cells in this study.

| Treatment | Polymer | Li deposited on the lower electrode [µm] | Li deposited on the upper electrode [µm] | Cycling current density [mA $cm^{-2}$] | Lithium passed per cycle [µm] |
|---|---|---|---|---|---|
| 1 | SEO(115-172) | 8.5 | 1.7 | 0.12 | 2.3 |
| 2 | SEO(200-222) | 39 | 19 | 0.175 | 3.4 |
| 3 | SEO(115-172) | 66 | 19 | 0.175 | 3.4 |

*X-ray microtomography.* The cells were imaged using hard X-ray microtomography at the Advanced Light Source at Lawrence Berkeley National Laboratory. Monochromatic hard X-rays with energy 22 keV at beamline 8.3.2 at the Advanced Light Source at Lawrence Berkeley National Laboratory illuminated the entire sample, and the X-ray shadow cast by the sample was converted into visible light using a scintillator. An optical microscope magnified this image and converted it into a digital image file. The sample was then rotated by a fraction of a degree and repeatedly imaged until 1,313 images were collected from the sample as it was rotated through 180°. After a series of data processing steps using the software Xi-

Cam[28], these shadow images were converted to cross-sectional slices that were then stacked together to render a 3D reconstruction of the cell. Cells were imaged in their original pouches at 2x, 4x, and/or 5x magnification, corresponding to a pixel size of approximately 3.25, 1.625, or 1.30 µm, respectively. Cross-sectional slices were stacked and rendered by the software ImageJ to be inspected for features of interest. Reconstructed three dimensional (3D) images were analyzed using the commercially available Avizo software package. Data acquisition and analysis builds on methods described by Harry et al. [5]

## RESULTS AND DISCUSSION

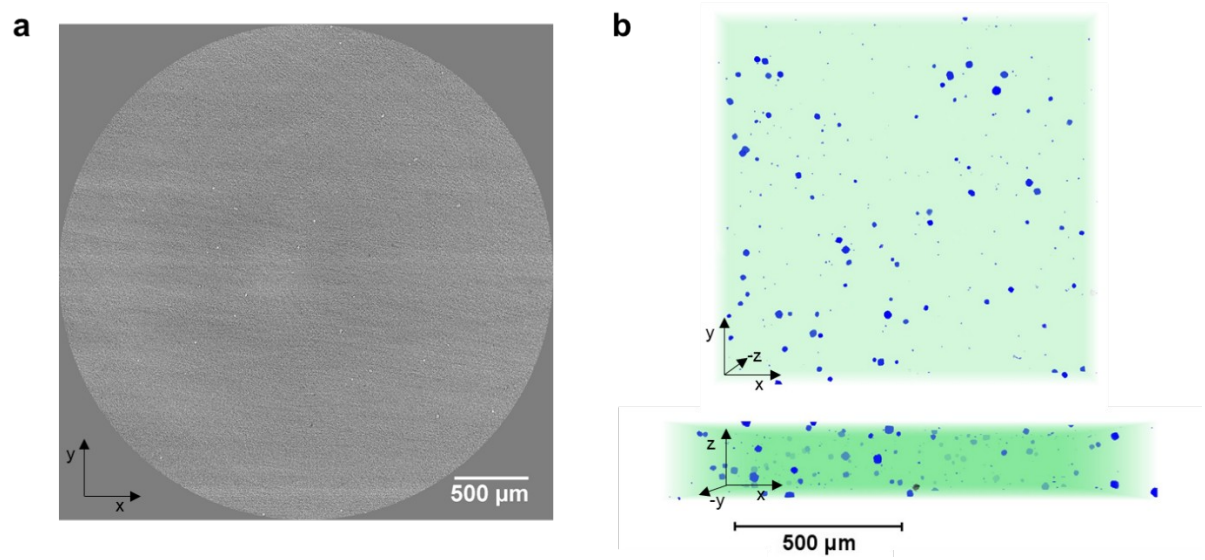


**Figure 1.** X-ray tomography results of a typical lithium electrode, showing the presence of impurity particles. (a) Cross-sectional slice through the lithium electrode in a symmetric cell as-fabricated showing bright, faceted objects that are impurity particles. (b) 3D rendering of a portion of a lithium electrode as-received with the impurity particles shown in blue.

Fig. 1 shows crystalline impurity particles embedded in lithium metal foil as-received, revealed by X-ray tomography. Fig. 1a shows an orthogonal cross-section through the xy plane (parallel to the plane of the lithium foil) of a reconstructed volume of lithium. The impurity particles are bright, faceted shapes in the darker gray metallic lithium. Fig. 1b shows two views of a volume within a typical lithium foil visualized in three dimensions. Here, the impurity particles have been highlighted in blue, and the metallic lithium is shown in light green. The visible particles vary in diameter between 2 and 30 µm. The number density of impurity particles greater than 2.6 µm in diameter is 1100 per $mm^3$. The number density of all impurity particles greater than 7.0 µm in diameter is 390 per $mm^3$.

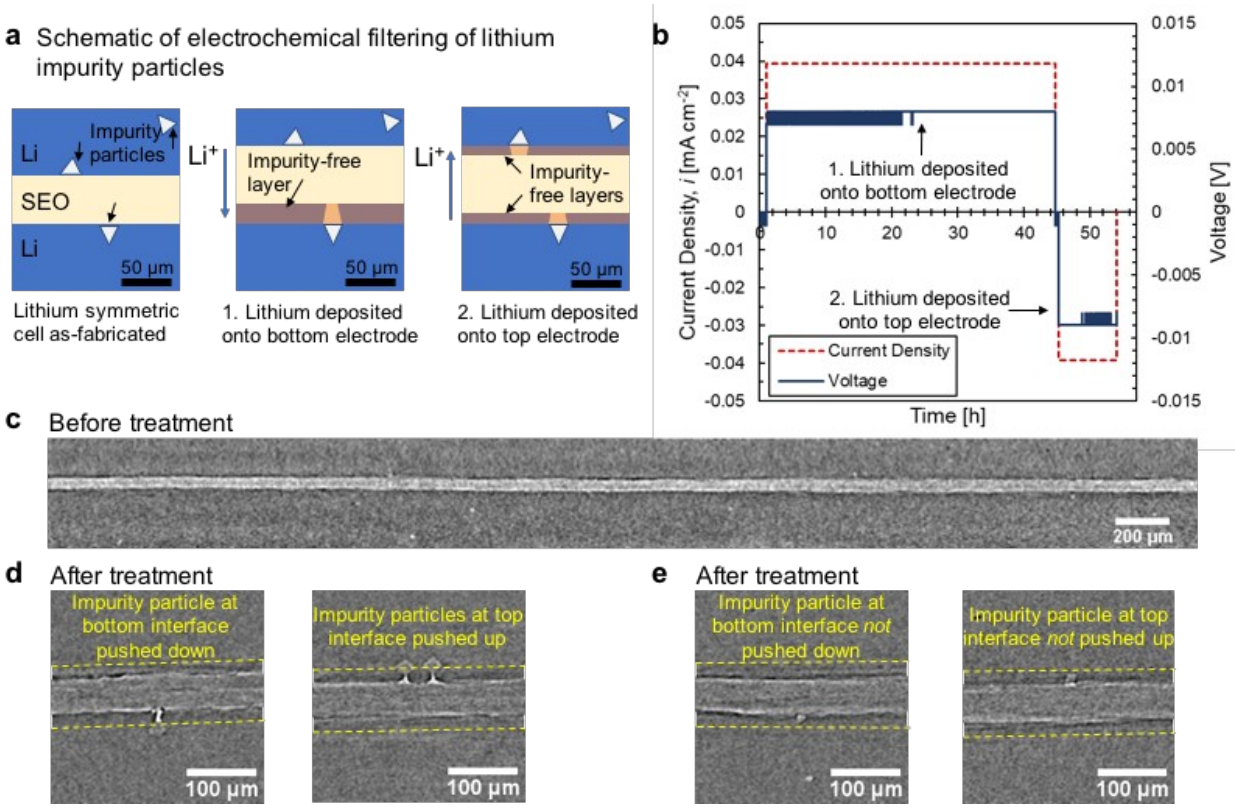


**Figure 2.** Strategy of the electrochemical filtering treatment to reduce the concentrations of impurity particles near the electrode-electrolyte interfaces. (a) Schematic of the electrochemical filtering treatment. After symmetric cell fabrication, some impurity particles, shown as white triangles, lie at the electrode-electrolyte interface. Step 1: with a sufficiently low current density, new planar lithium, highlighted in orange, is deposited on to the bottom electrode to create a layer free of impurity particles. Step 2: by reversing the direction of current, planar lithium is plated on to the upper electrode, such that both electrodes now have a layer of impurity-free lithium at the electrode-electrolyte interface. (b) Current density and voltage of one electrochemical filtering treatment over time (Treatment 1). Lithium was deposited on to the lower electrode at 0.04 mA $cm^{-2}$ for 43.75 h (8.5 µm of Li calculated) and deposited back on to the upper electrode at the same current density for 8.75 h (1.7 µm of Li calculated). The voltage oscillations reflect the precision of the Maccor cycler. (c) Slice through a reconstructed volume of a symmetric cell after 14 conditioning cycles. No inhomogeneities were observed at the interfaces. (d) Slices through a

reconstructed volume of the symmetric cell in Fig. 2c after an electrochemical filtering treatment. This cell received Treatment 2; details of the treatment may be found in Table 2. Yellow dashed lines indicate the calculated height of filtered lithium after the treatment. Impurity particles are visibly pushed away from the electrode-electrolyte interface, resulting in void defects. (e) Slices through a different area of the cell shown in Fig. 2c and 2d. Yellow dashed lines indicate the calculated height of filtered lithium after the treatment. Some impurity particles still remain adhered to the polymer electrolyte at the electrode-electrolyte interface.

Fig. 2 describes the strategy and results of the electrochemical filtering treatment applied to reduce the concentration of impurity particles near the electrode-electrolyte interface. We hypothesized that nucleation of defective deposition could be suppressed if impurity particles were not present in the layers of lithium cycled. Fig. 2a is a schematic of the electrochemical filtering treatment. During step 1, lithium is deposited on to the bottom electrode. With a sufficiently low current density, new planar lithium, highlighted in orange, is deposited on to the bottom electrode. However, due to the insulating nature of the impurity particle, electrodeposition immediately above the particle is hindered, leading to a void defect. Since the impurity particles are uncharged and insulating, we expect to create a layer free of impurity particles on the bottom electrode. During step 2, the direction of current is reversed such that a fraction of the planar impurity-free lithium is plated on to the upper electrode. After executing these 2 steps, both electrodes have a layer of impurity-free lithium at the electrode-electrolyte interface. Fig. 2b shows typical voltage versus time data during the electrochemical filtering treatment (Treatment 1). After a one-hour rest for temperature equilibration, a current density of 0.04 mA $cm^{-2}$ was imposed for 43.75 h (a calculated height of 8.5 µm of Li). Then, a current density of -0.04 mA $cm^{-2}$ was

imposed for 8.75 h (a calculated height of 1.7 μm of Li). We note that at this magnitude of current density, lithium deposition is shown to be planar.[10] The voltage versus time data obtained from other treatments is similar to that shown in Fig. 2b, except for duration of each step. Fig. 2c shows a slice through a reconstructed cell volume after conditioning cycles but before any treatment was applied, visualized by X-ray tomography. No inhomogeneities were observed within the cell. Fig. 2d shows two slices from a reconstructed 3D volume showing a decreased concentration of impurity particles near the electrode-electrolyte interface after Treatment 2 was applied. The dashed yellow lines indicate the calculated height of lithium deposited on each electrode in this cell (19 μm). Bright lines stretching from the impurity particle toward the electrolyte represent voids in the lithium electrode that are filled with electrolyte which we call void defects – inhomogeneous deposition where no lithium was deposited on to the electrically insulating impurity particle.[8,10] We use the term “defect” to refer to all forms of non-uniform lithium plating (e.g., Fig. 2). This is in contrast to our use of the term “impurity particle” to refer to foreign crystalline objects in the as-received lithium foil (Fig. 1). Fig. 2e shows two slices from a reconstructed 3D volume showing impurity particles that remain adhered to the electrode-electrolyte interfaces (top and bottom) after treatment. The electrochemical filtering treatment results in an 85% reduction in the concentration of impurity particles in the lithium electrode near the interfaces.

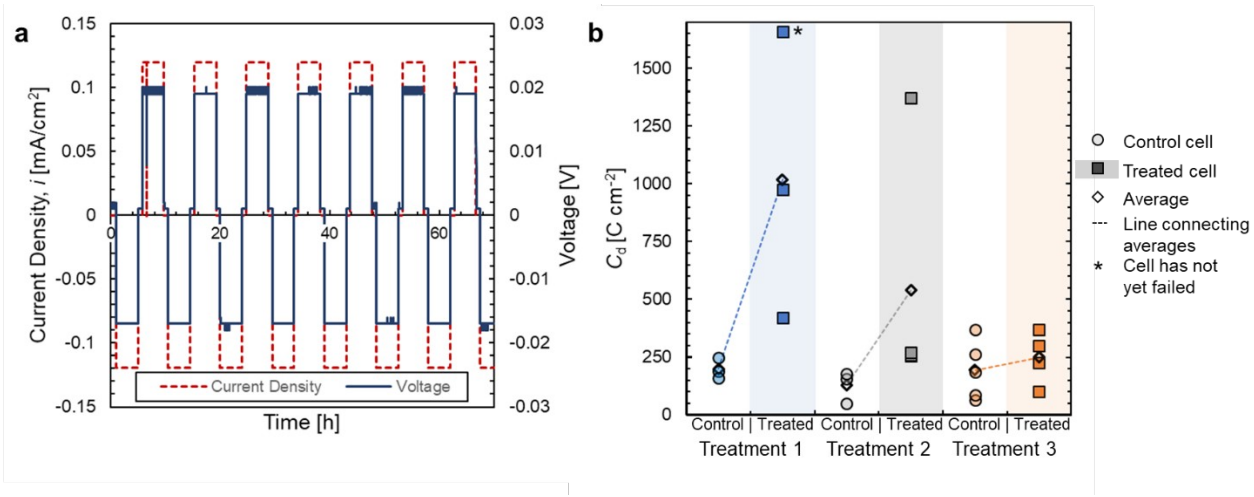


**Figure 3.** Galvanostatic cell cycling example and results. (a) Current density and voltage of the first cycles at 0.12 mA $cm^{-2}$ for a typical cell in Treatment 1. (b) Charge passed before failure, $C_d$, for treated cells and their corresponding control cells. Details of the electrochemical filtering treatment are given in Table 2. The transparent circles indicate control cells, while the filled-in squares indicate treated cells. Hollow diamonds indicate the average of cells in the column. Dashed lines connect the averages of control and treated cells in each group. The asterisk indicates a cell which had not failed at the end of the experiment (4500 hours).

Fig. 3 shows an example of galvanostatic cell cycling and results. Fig. 3a shows current density applied and voltage response of a cell during cycling at 0.12 mA $cm^{-2}$. A precipitous drop in voltage was taken as the signal of a short-circuit caused by an electrolyte-spanning lithium protrusion. Fig. 3b shows the charge passed before failure, $C_d$, calculated from the cycles before failure and the current density applied, for control and treated cells. Details of the electrochemical filtering treatment are given in Table 2. $C_d$ is greater for treated cells in every case, but the increase in average lifetime decreases as more lithium is passed during the treatment step. In the control cells, $C_d$ varies from 50-400 C $cm^{-2}$. In the case of

Treatment 1, $C_d$ values as high as 1650 C cm-2 were recorded. On average, Treatment 1 results in a fivefold increase in cycle life.

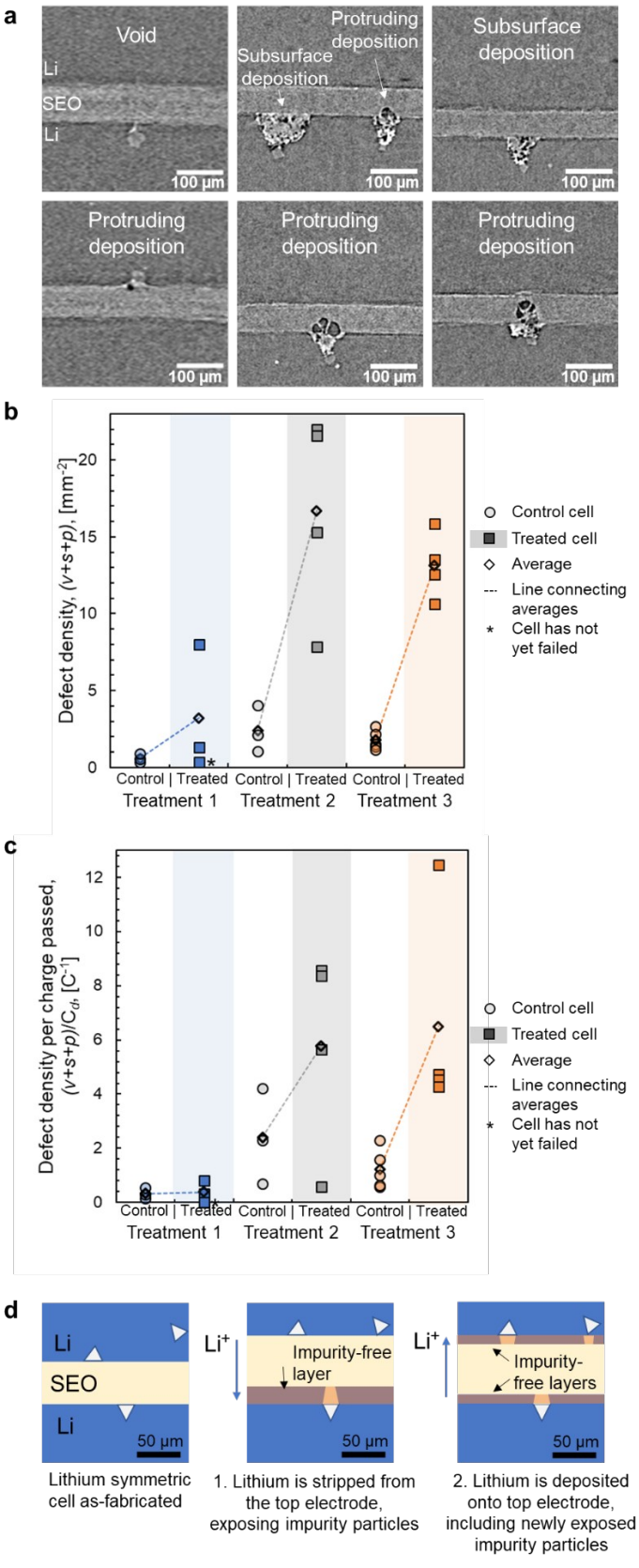
a
Void
Li
SEO
Li
100 µm
Protruding deposition
Subsurface deposition
Subsurface deposition
Protruding deposition
Protruding deposition
Protruding deposition
b
Defect density, (v+s+p), [mm-2]
0
5
10
15
20
Control | Treated
Treatment 1
Treatment 2
Treatment 3
Control cell
Treated cell
Average
Line connecting averages
Cell has not yet failed
c
Defect density per charge passed, (v+s+p)/Cd, [C-1]
0
2
4
6
8
10
12
d
Li
SEO
Li
50 µm
Li+
Impurity-free layer
Impurity-free layers
Lithium symmetric cell as-fabricated
1. Lithium is stripped from the top electrode, exposing impurity particles
2. Lithium is deposited onto top electrode, including newly exposed impurity particles

**Figure 4.** Defective deposition events in cycled cells. (a) Slices through reconstructed volumes of failed cells. These slices demonstrate the variety of morphologies of defective deposition. Every instance of defective deposition is associated with an impurity particle. Examples of voids, subsurface deposition, and protruding deposition are labeled. (b) Plot of the defect density per area for control and treated cells, $(v+s+p)$: this is the summed areal density of void, $v$, subsurface, $s$, and protruding deposition, $p$, per mm$^2$. (c) Plot of the defect density per area divided by charge passed before failure for control and treated cells, $(v+s+p)/C_d$. (d) Schematic suggesting an explanation for the higher areal density of defective deposition observed in treated cells. Step 1: with a sufficiently low current density, new planar lithium, highlighted in orange, can be deposited on to the bottom electrode to create a layer free of impurity particles. During the course of this deposition, additional impurity particles are revealed at the upper electrode-electrolyte interface. Step 2: by reversing the direction of current, planar lithium is plated on to the upper electrode. Each of the newly exposed impurity particles on the upper electrode creates a void in the planar deposition of lithium. During cycling, these voids lead to subsurface and protruding deposition.

Fig. 4a shows examples of a variety of defective deposition events in control and treated cells. Examples of voids, subsurface deposition, and protruding deposition are labeled. We define subsurface defects as those restricted to the region below the electrode-electrolyte interface, and protrusion defects as those which protrude into the electrolyte. The deposition defect may vary in size from less than 10 μm to greater than 100 μm. Subsurface and protrusion defects contain both trapped electrolyte (bright) and lithium globules (dark). A short-circuit occurs when a defect spans the electrolyte and contacts the opposite electrode. Fig. 4b plots the areal defect density for control and treated cells, $(v+s+p)$: this is the summed areal

density of void, $v$, subsurface, $s$, and protruding deposition, $p$, per mm$^2$. Treated cells have a significantly higher density of defective deposition events. The increase in defect density is smallest in the batch of cells with the least amount of lithium passed during filtering (Treatment 1). In principle, the higher defect densities in treated cells could arise because they were cycled longer. To consider this effect, Fig. 4c plots the areal defect density for control and treated cells normalized by charge passed before failure, $(v+s+p)/C_d$. Fig. 4c shows that treated cells have a higher normalized areal defect density. The data in Fig. 4b and 4c are surprising because one expects cells with higher cycle life to exhibit lower areal defect densities. A reason for the trends presented in Fig. 4b and 4c is proposed in Fig. 4d: the schematic is similar to Fig. 2a. The creation of an impurity-free layer on the bottom electrode concentrates impurities on the top electrode. As the thickness of the impurity-free layer is increased, the concentration of impurity particles on the top electrode also increases. Despite the increased defect density, treated cells exhibit a longer cycle life.

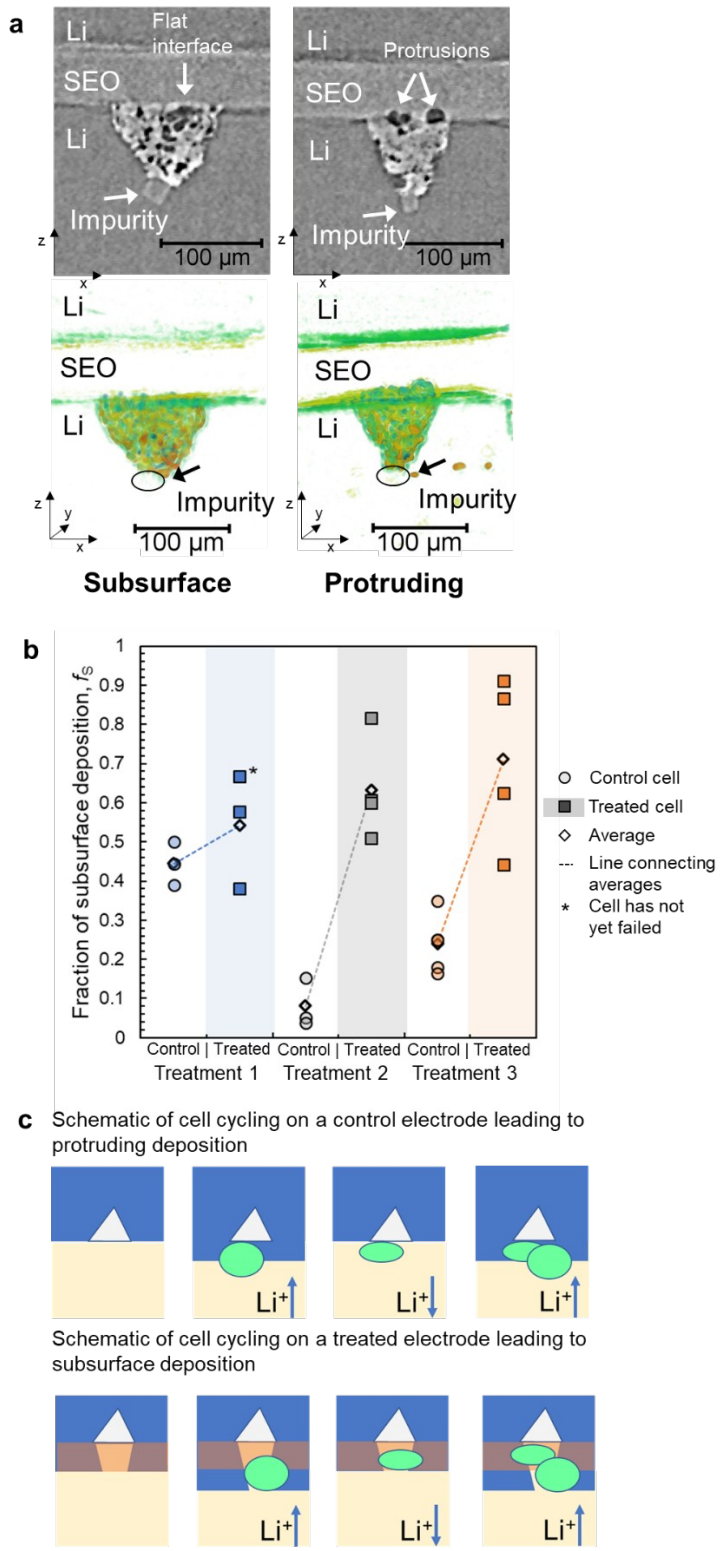


**Figure 5.** Subsurface and protruding defects in control and treated cells. (a) Slices through failed cells showing a subsurface deposition defect (left) and a slightly protruding deposition

defect (right). Large protrusions are also observed, as documented in Fig. 4. Volume renderings of the same defects are shown below each slice. (b) Plot of $f_s$, the fraction of subsurface deposition defects for treated and untreated cells. (c) Schematic of a control (top) and treated (bottom) cell proceeding through half-cycles. Impurity particles are represented by white triangles. A layer of impurity-free lithium on the treated cell is highlighted in orange. The electrolyte is represented with light yellow. Each panel moving right represents an additional half-cycle of charge passed in the cell. Planar lithium, shown in blue, and defective lithium, shown in green, is stripped or plated during each half-cycle. Over the course of two cycles, the defective lithium grows in volume. In the control cell, the defective lithium protrudes into the electrolyte, while in the treated cell, the defective lithium is buried under the electrode-electrolyte interface.

The morphology of deposition defects affects cycle life: this is examined in Fig. 5. Fig. 5a defines subsurface and protruding morphology. Both defects are nucleated on impurity particles and comprise a collection of globular lithium objects (dark) encapsulated by electrolyte (bright). On the left side, we show a slice through a tomogram of a subsurface defect and a volume rendering of the same. In this case, the globular lithium does not protrude above the electrode-electrolyte interface. On the right side, we show a slice through a tomogram of a protruding defect and a volume rendering of the same. In this case, the globular lithium protrudes slightly above the electrode-electrolyte interface. We show this example to indicate that X-ray tomography enables distinguishing between subsurface and protruding defects; examples of defects that penetrate more deeply into the electrolyte are shown in Fig. 4. We define the fraction of subsurface deposition defects, $f_s$, as

$$f_s = \frac{s}{p+s} \quad (1)$$

Fig. 5b shows the effect of lithium filtering treatment on $f_s$. It is evident that the fraction of subsurface deposition is significantly higher in treated cells. The short-circuiting of cells must be related to the fraction of protruding defects ($1-f_s$). As the cell is cycled, one expects subsurface defects to transform into protruding defects and $f_s$ will decrease. $f_s$ is larger in the treated cells in spite of the fact that the cycle life of treated cells is higher than that of untreated cells. Moreover, the difference is more dramatic in cells with larger volumes of lithium passed during the filtering step. A possible mechanism for this is shown in Fig. 5c. The top row represents a control cell during cycling, and the bottom row represents a treated cell. Each panel moving right represents an additional half-cycle of charge passed in the cell. In the control cell, a multiglobular defect grows at an impurity particle, while in the treated cell, a multiglobular defect grows within a void defect created during the lithium filtering treatment. The proposed mechanism is only effective when the electrolyte is a rigid solid which provides mechanical resistance to the growth of protrusions.

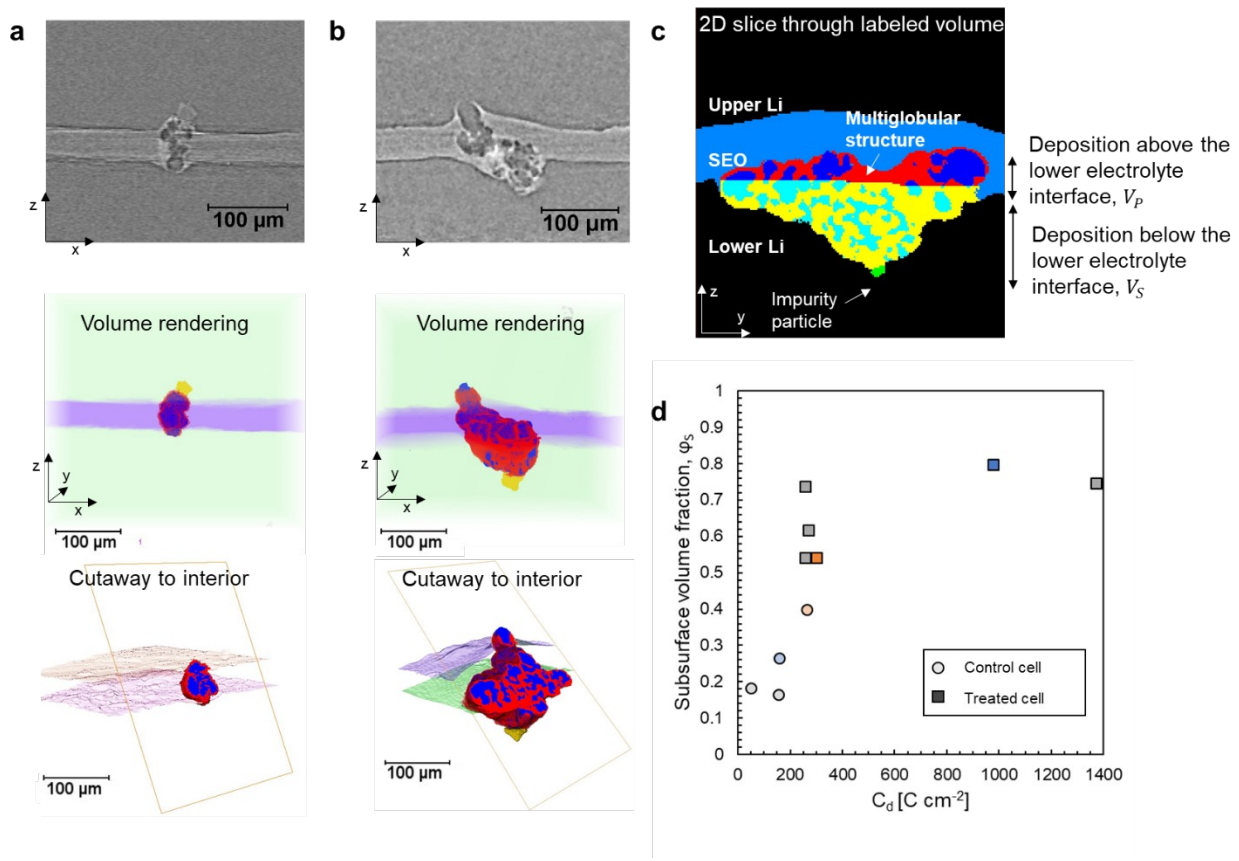


**Figure 6.** Differences in morphology between short-circuit globules in control and treated cells. (a) A representative short-circuit multiglobular structure from a control cell. In the top row, a slice through a reconstructed 3D volume. In the middle row, a volume rendering of the structure shown above. In the bottom row, a slice through the volume rendering of the structure revealing the internal network of globular lithium surrounded by electrolyte. (b) A representative short-circuit multiglobular structure from a treated cell. The top, middle, and bottom images are as described in (a). (c) A slice through the multiglobular structure in (b) showing labeled sections of multiglobular lithium and surrounding electrolyte. Above the electrolyte, the globular lithium is labeled in dark blue and the encapsulating electrolyte is labeled in red. Below the electrolyte, the globular lithium is labeled in light blue and the encapsulating electrolyte is labeled in yellow. The volumes of the multiglobular structure above and below the electrode-electrolyte interface are represented by $V_P$ and $V_S$,

respectively. The impurity particle is labeled in green. The subsurface volume fraction, $\varphi_S$, is defined $\varphi_S = \frac{V_S}{V_P + V_S}$. (d) Plot of subsurface volume fraction, $\varphi_S$, as a function of charge passed before failure, $C_d$. The transparent circles indicate control cells, while the filled-in squares indicate treated cells. Blue symbols indicate Treatment 1 cells, gray symbols indicate Treatment 2 cells, and orange symbols indicate Treatment 3 cells.

Quantitative proof that increased subsurface deposition leads to longer cycle life lies in the visualization of the multiglobular structures that short-circuited each cell, shown in Fig. 6. Fig. 6a and 6b compare the morphologies of multiglobular shorts through control and treated cells. The top image is an orthogonal slice through the structure, the middle shows a volume rendering, and the bottom shows a volume rendering with a cutaway to the interior. In the volume renderings, the multiglobular lithium is shown in dark blue, while the encapsulating electrolyte is shown in red. The electrolyte is represented by purple, the impurity is shown in yellow, and the lithium metal is shown as light green. It is evident that the short-circuit structure in the treated cell has both a larger volume and a larger fraction of its bulk buried under the electrode-electrolyte interface. Each of these factors could account for longer cycle life of the treated cell. To visualize the volume of the structure, voxels were labeled with a material, which is shown color-coded in Fig. 6c. Fig. 6c shows a 2D slice through the labeled multiglobular structure. Above the electrolyte, the globular lithium is labeled in dark blue and the encapsulating electrolyte is labeled in red. Below the electrolyte, the globular lithium is labeled in light blue and the encapsulating electrolyte is labeled in yellow. The volumes of the multiglobular structure above and below the electrode interface are represented by

$V_P$ and $V_S$, respectively. The impurity particle is labeled in green. It is evident that the multiglobular structure consists of a network of globular lithium with interpenetrating electrolyte. We define the volume fraction of the structure that is subsurface, $\varphi_S$, as

$$\varphi_S = \frac{V_S}{V_P + V_S}. \quad (2)$$

In Fig. 6d, $\varphi_S$ is plotted as a function of $C_d$, charge passed before failure. All Treatment 2 cells where a short-circuit was identified are included in the plot. One control and one treated cell from Treatments 1 and 3 are also included. Short-circuiting multiglobular structures in treated cells have a significantly higher subsurface volume fraction than control cells. This difference is especially pronounced for cells with a larger amount of charge passed before failure.

We note that a related consequence of increased subsurface volume in the short-circuiting multiglobular structures of treated cells is that the impurity particle has been pushed far below the interface. For the structures shown in Fig. 6, the impurity particle in the control cell lies 10 μm below the interface (having begun at 0 μm) and the impurity particle in the treated cell lies 40 μm below the interface (having begun between 0 and 19.4 μm away). This suggests that creep of lithium may occur as the impurity is pushed below the interface. Further studies are required to elucidate the nature of this deformation, which depends on the nonlinear mechanical properties of metallic lithium.[29–33]

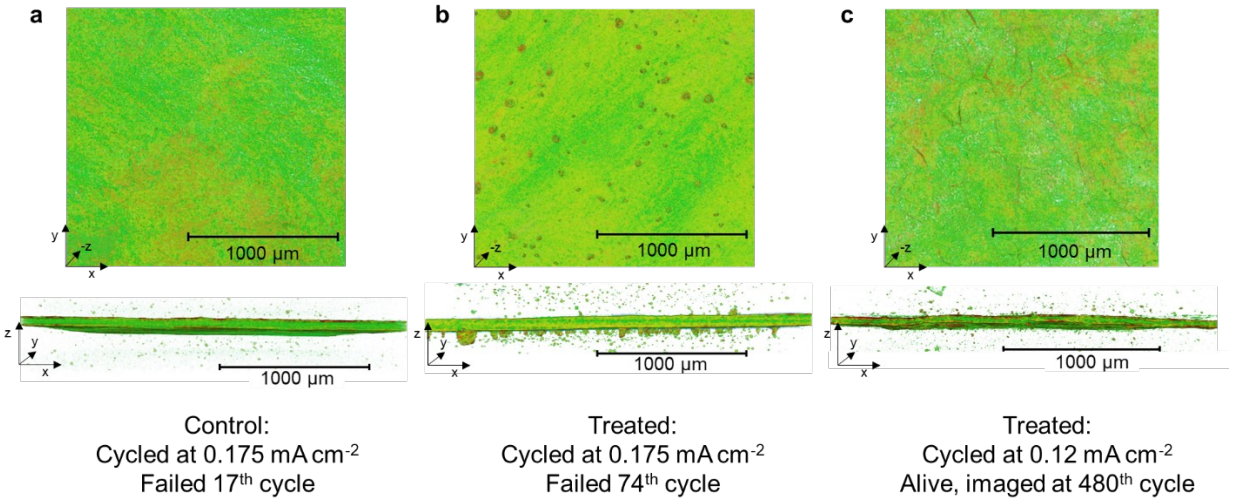


**Figure 7.** Volume renderings of the electrolyte in three types of cells. The lithium is largely transparent such that only the electrolyte and deposition defects are visible. (a) Control cells have relatively few deposition defects, and protrusions short the cell quickly. (b) Treated cells have more deposition defects, but these defects are more likely to be subsurface – subsurface deposition does not shorten cell life. Defects are visible as yellow-orange protrusions below and above the electrolyte. (c) The cell processed using Treatment 1 that did not fail. Most of the defects are voids nucleated at grain boundaries in the lithium metal, visible in the volume rendering as darker lines. In this cell, deposition defects are sparse and the lifetime so far is more than an order of magnitude higher than that of the untreated cells.

A visual summary of the dominant cell behaviors observed in this study is shown in Fig. 7. Each image represents a volume rendering of the electrolyte within a symmetric cell. The metallic lithium above and below the electrolyte has been made transparent. Specks within the lithium indicate impurity particles – there are some contrast and resolution differences between each cell due to cell and beam differences during imaging. Fig. 7a shows a control cell which was cycled at 0.175 mA $cm^{-2}$ and failed after the $17^{th}$ cycle. The electrolyte appears unmarred despite

the failure of the cell. We observed that control cells have a smaller areal density of defects (Fig. 4), but protrusions short the cell quickly (Fig. 3). The defect that caused cell failure in the cell shown in Fig. 7a lies outside the visualized region in the figure. Fig. 7b shows a treated cell which was cycled at 0.175 mA $cm^{-2}$ and failed after the $74^{th}$ cycle. Yellow-orange lumps above and below the electrolyte seen in the edge view of Fig. 7b indicate subsurface features of defects, where the electrolyte invades the lithium (Fig. 5). These subsurface features are also evident in the top view of Fig. 7b. Fig. 7c shows a treated cell which was cycled at 0.12 mA $cm^{-2}$ which did not fail and was imaged after the $480^{th}$ cycle. The side view of this cell is similar to that in Fig. 7a, in spite of the large difference in cycle life (17 versus 480 cycles). The deposition defects in Fig. 7c are only evident in the top view, where we observe the presence of dark lines. We posit these lines represent shallow voids that are formed on grain boundaries in the lithium metal. For reasons that are unclear, the density of globular defects in this cell was very low (0.1 $mm^{-2}$). It is evident that in the case of this cell, the electrochemical filtering step was the most effective. This cell's lifetime was more than an order of magnitude higher than that of the untreated cells.

## CONCLUSION

Impurity particles in lithium metal have been implicated in the nucleation of multiglobular structures which grow and short-circuit lithium symmetric cells containing a solid block copolymer electrolyte. An “electrochemical filtering” treatment was performed on these cells in order to reduce the concentration of these impurity particles at the electrode-electrolyte interface. A thick layer of lithium was electrodeposited during the first treatment step and a fraction of this layer was deposited back on to the opposite electrode in the second treatment step. The cells were cycled and imaged using X-ray tomography to determine the effect of this treatment on cell lifetime and lithium deposition morphology. Depending on the treatment details, average charge passed before failure was improved by 30-400%. For a cell in which the treatment was most effective, cycle life was increased by more than an order of magnitude and the measured defect density was negligible.

While the treatment resulted in a significant reduction in the concentration of impurity particles at the electrode-electrolyte interfaces, the cycled lithium layers contained void defects. The treatment that was most effective was the one where the thickness of the deposited lithium during the first treatment step was the smallest. In general, treated cells had a higher areal density of defects, but a majority of these defects were confined within the electrodes. In contrast, most of the defects seen in the control cells were protrusions that invaded the electrolyte phase. For all but one cell, increased lifetime due to electrochemical filtering was not due to a reduction in defect density, but rather due to the differences in defect morphology. Further improvements in the quality of the cycled lithium layer (e.g.,

eliminating void defects and adhered impurity particles shown in Fig. 2) may result in even longer cycle life.

## NOMENCLATURE

| Symbol | |
|---|---|
| $i$ | Current density [mA $cm^{-2}$] |
| $V$ | Voltage [V] |
| $C_d$ | Charge passed before failure [C $cm^{-2}$] |
| $v$ | Areal density of void defects [$mm^{-2}$] |
| $s$ | Areal density of subsurface defects [$mm^{-2}$] |
| $p$ | Areal density of protrusion defects [$mm^{-2}$] |
| $f_s$ | Fraction of defects subsurface, $\frac{S}{P+S}$ |
| $V_S$ | Volume of defect subsurface (below the electrode-electrolyte interface) [$\mu m^3$] |
| $V_P$ | Volume of defect protruding (above the electrode-electrolyte interface) [$\mu m^3$] |
| $\varphi_S$ | Volume fraction of the defect that is subsurface, $\frac{V_S}{V_P+V_S}$ |

## AUTHOR INFORMATION


### Corresponding Author

*nbalsara@berkeley.edu


### Notes

The authors declare no competing financial interest.

## ACKNOWLEDGMENTS

This work was supported by the Assistant Secretary for Energy Efficiency and Renewable Energy, Office of Vehicle Technologies of the U.S. Department of Energy under Contract DE-AC02-05CH11231 under the Battery Materials Research Program. Hard X-ray experiments were performed at the Advanced Light Source which is supported by the Director, Office of Science, Office of Basic Energy Sciences, of the U.S. Department of Energy under Contract No. DE-AC02-05CH11231. JAM was supported by a National Science Foundation Graduate Research Fellowship DGE-2752814. LF acknowledges funding from the Energy & Biosciences Institute through the EBI-Shell program. WSL was supported by a National Science Foundation Graduate Research Fellowship DGE-1106400.

## REFERENCES


(1) Eastwood, D. S.; Bradley, R. S.; Tariq, F.; Cooper, S. J.; Taiwo, O. O.; Gelb, J.; Merkle, A.; Brett, D. J. L.; Brandon, N. P.; Withers, P. J.; Lee, P. D.; Shearing, P. R. The Application of Phase Contrast X-Ray Techniques for Imaging Li-Ion Battery Electrodes. *Nucl. Instruments Methods Phys. Res. B* **2014**, *324*, 118–123.

(2) Sun, F.; Zielke, L.; Markötter, H.; Hilger, A.; Zhou, D.; Moroni, R.; Zengerle, R.; Thiele, S.; Banhart, J.; Manke, I. Morphological Evolution of Electrochemically Plated/Stripped Lithium Microstructures Investigated by Synchrotron X-Ray Phase Contrast Tomography. *ACS Nano* **2016**, *10* (8), 7990–7997.

(3) Taiwo, O. O.; Finegan, D. P.; Paz-Garcia, J. M.; Eastwood, D. S.; Bodey, A. J.; Rau, C.; Hall, S. A.; Brett, D. J. L.; Lee, P. D.; Shearing, P. R. Investigating the Evolving Microstructure of Lithium Metal Electrodes in 3D Using X-Ray Computed Tomography. *Phys. Chem. Chem. Phys.* **2017**, *19* (33), 22111–22120.

(4) Frisco, S.; Liu, D. X.; Kumar, A.; Whitacre, J. F.; Love, C. T.; Swider-Lyons, K. E.; Litster, S. Internal Morphologies of Cycled Li-Metal Electrodes Investigated by Nano-Scale Resolution X-Ray Computed Tomography. *ACS Appl. Mater. Interfaces* **2017**, *9* (22), 18748–18757.

(5) Harry, K. J.; Hallinan, D. T.; Parkinson, D. Y.; Macdowell, A. A.; Balsara, N. P. Detection of Subsurface Structures underneath Dendrites Formed on Cycled Lithium Metal Electrodes. *Nat. Mater.* **2013**, *13* (1), 69–73.

(6) Devaux, D.; Harry, K. J.; Parkinson, D. Y.; Yuan, R.; Hallinan, D. T.; MacDowell,

A. A.; Balsara, N. P. Failure Mode of Lithium Metal Batteries with a Block Copolymer Electrolyte Analyzed by X-Ray Microtomography. *J. Electrochem. Soc.* **2015**, *162* (7), A1301–A1309.

(7) Schauser, N. S.; Harry, K. J.; Parkinson, D. Y.; Watanabe, H.; Balsara, N. P. Lithium Dendrite Growth in Glassy and Rubbery Nanostructured Block Copolymer Electrolytes. *J. Electrochem. Soc.* **2015**, *162* (3), 398–405.

(8) Harry, K. J.; Liao, X.; Parkinson, D. Y.; Minor, A. M.; Balsara, N. P. Electrochemical Deposition and Stripping Behavior of Lithium Metal across a Rigid Block Copolymer Electrolyte Membrane. *J. Electrochem. Soc.* **2015**, *162* (14), A2699–A2706.

(9) Harry, K. J.; Higa, K.; Srinivasan, V.; Balsara, N. P. Influence of Electrolyte Modulus on the Local Current Density at a Dendrite Tip on a Lithium Metal Electrode. *J. Electrochem. Soc.* **2016**, *163* (10), 2216–2224.

(10) Maslyn, J. A.; Loo, W. S.; McEntush, K. D.; Oh, H. J.; Harry, K. J.; Parkinson, D. Y.; Balsara, N. P. Growth of Lithium Dendrites and Globules through a Solid Block Copolymer Electrolyte as a Function of Current Density. *J. Phys. Chem. C* **2018**, *122*, 26797–26804.

(11) Monroe, C.; Newman, J. Dendrite Growth in Lithium/Polymer Systems. *J. Electrochem. Soc.* **2003**, *150* (10), A1377–A1384.

(12) Stone, G. M.; Mullin, S. A.; Teran, A. A.; Hallinan, D. T.; Minor, A. M.; Hexemer, A.; Balsara, N. P. Resolution of the Modulus versus Adhesion Dilemma in Solid Polymer Electrolytes for Rechargeable Lithium Metal Batteries. *J. Electrochem. Soc.* **2012**, *159* (3), A222–A227.

(13) Ganser, M.; Hildebrand, F. E.; Klinsmann, M.; Hanauer, M.; Kamlah, M.; Mcmeeking, R. M. An Extended Formulation of Butler-Volmer Electrochemical Reaction Kinetics Including the Influence of Mechanics. **2019**, *166* (4).

(14) Fan, L.; Wei, S.; Li, S.; Li, Q.; Lu, Y. Recent Progress of the Solid-State Electrolytes for High-Energy Metal-Based Batteries. *Adv. Energy Mater.* **2018**, *8*, 1702657 (1-31).

(15) Zhang, X.; Chen, X.; Cheng, X.; Li, B.; Shen, X.; Yan, C.; Huang, J.; Zhang, Q. Highly Stable Lithium Metal Batteries Enabled by Regulating the Solvation of Lithium Ions in Nonaqueous Electrolytes. *Angew. Chem. Int. Ed. Engl.* **2018**, *57*, 5301–5305.

(16) Zhou, J.; Qian, T.; Liu, J.; Wang, M.; Zhang, L.; Yan, C. High-Safety All-Solid-State Lithium-Metal Battery with High-Ionic-Conductivity Thermoresponsive Solid Polymer Electrolyte. *Nano Lett.* **2019**, *19*, 3066–3073.

(17) Cao, C.; Li, Y.; Feng, Y.; Peng, C.; Li, Z.; Feng, W. A Solid-State Single-Ion Polymer Electrolyte with Ultrahigh Ionic Conductivity for Dendrite-Free Lithium Metal Batteries. *Energy Storage Mater.* **2019**, *19*, 401–407.

(18) Kazyak, E.; Wood, K. N.; Dasgupta, N. P. Improved Cycle Life and Stability of Lithium Metal Anodes through Ultrathin Atomic Layer Deposition Surface Treatments. *Chem. Mater.* **2015**, *27*, 6457–6462.

(19) Lee, H.; Lee, D. J.; Kim, Y.; Park, J.; Kim, H. A Simple Composite Protective Layer Coating That Enhances the Cycling Stability of Lithium Metal Batteries. *J. Power Sources* **2015**, *284*, 103–108.

(20) Liu, W.; Lin, D.; Pei, A.; Cui, Y. Stabilizing Lithium Metal Anodes by Uniform Li-

Ion Flux Distribution. *J. Am. Chem. Soc.* **2016**, *138*, 15443–15450.

(21) Chen, L.; Connell, J. G.; Nie, A.; Huang, Z.; Zavadil, K. R.; Klavetter, K. C.; Yuan, Y.; Shahbazian-yassar, R.; Libera, J. A.; Mane, U.; Elam, W. Lithium Metal Protected by Atomic Layer Deposition Metal Oxide for High Performance Anodes. *J. Mater. Chem. A* **2017**, *5*, 12297–12309.

(22) Becking, J.; Gröbmeyer, A.; Kolek, M.; Rodehorst, U.; Schulze, S.; Winter, M.; Bieker, P.; Stan, M. C. Lithium-Metal Foil Surface Modification: An Effective Method to Improve the Cycling Performance of Lithium-Metal Batteries. *Adv. Mater. Interfaces* **2017**, No. 4, 1700166.

(23) Tang, W.; Yin, X.; Chen, Z.; Fu, W.; Ping, K.; Wesley, G. Chemically Polished Lithium Metal Anode for High Energy Lithium Metal Batteries. *Energy Storage Mater.* **2018**, *14*, 289–296.

(24) Meyerson, M. L.; Sheavly, J. K.; Dolocan, A.; Griffin, M. P.; Pandit, A. H.; Rodriguez, R.; Stephens, R. M.; Vanden Bout, D. A.; Heller, A.; Mullins, C. B. The Effect of Local Lithium Surface Chemistry and Topography on Solid Electrolyte Interphase Composition and Dendrite Nucleation. *J. Mater. Chem. A* **2019**, *7*, 14882–14894.

(25) Quirk, R. P.; Kim, J.; Kausch, C.; Chun, M. Butyllithium-Initiated Anionic Synthesis of Well-Defined Poly(Styrene-Block-Ethylene Oxide) Block Copolymers with Potasium Salt Additives. *Polym. Int.* **1996**, *39* (1), 3–10.

(26) Hadjichristidis, N.; Iatrou, H.; Pispas, S.; Pitsikalis, M. Anionic Polymerization: High Vacuum Techniques. *J. Polym. Sci. Part A Polym. Chem.* **2000**, *38*, 3211–3234.

(27) Singh, M.; Odusanya, O.; Wilmes, G. M.; Eitouni, H. B.; Gomez, E. D.; Patel, A. J.; Chen, V. L.; Park, M. J.; Fragouli, P.; Iatrou, H.; Hadjichristidis, N.; Cookson, D.; Balsara, N. P. Effect of Molecular Weight on the Mechanical and Electrical Properties of Block Copolymer Electrolytes. *Macromolecules* **2007**, *40* (13), 4578–4585.

(28) Pandolfi, R. J.; Allan, D. B.; Arenholz, E.; Barroso-Luque, L.; Campbell, S. I.; Caswell, T. A.; Blair, A.; De Carlo, F.; Fackler, S.; Fournier, A. P.; Freychet, G.; Fukuto, M.; Gursoy, D.; Jiang, Z.; Krishnan, H.; Kumar, D.; Kline, R. J.; Li, R.; Liman, C.; Marchesini, S.; Ren, F.; Sahoo, S.; Strzalka, J.; Sunday, D.; Tassone, C. J.; Ushizima, D.; Venkatakrishnan, S.; Yager, K. G.; Zwart, P.; Sethian, J. A.; Hexemer, A. Xi-Cam: A Versatile Interface for Data Visualization and Analysis. *J. Appl. Synchrotron Radiat.* **2018**, *25*, 1261–1270.

(29) Xu, C.; Ahmad, Z.; Aryanfar, A.; Viswanathan, V.; Greer, J. R. Enhanced Strength and Temperature Dependence of Mechanical Properties of Li at Small Scales and Its Implications for Li Metal Anodes. *Proc. Natl. Acad. Sci.* **2017**, *114* (1), 57–61.

(30) Herbert, E. G.; Hackney, S. A.; Dudney, N. J.; Phani, P. S. Nanoindentation of High Purity Vapor Deposited Lithium Films: The Elastic Modulus. *J. Mater. Res.* **2018**, *33*, 1334–1345.

(31) Herbert, E. G.; Hackney, S. A.; Dudney, N. J.; Thole, V.; Phani, P. S. Nanoindentation of High Purity Vapor Deposited Lithium Films: A Mechanistic Rationalization of Diffusion-Mediated Flow. *J. Mater. Res.* **2018**, *33*, 1346–1359.

(32) Herbert, E. G.; Hackney, S. A.; Dudney, N. J.; Thole, V.; Phani, P. S.

Nanoindentation of High Purity Vapor Deposited Lithium Films: A Mechanistic Rationalization of the Transition from Diffusion to Dislocation-Mediated Flow. *J. Mater. Res.* **2018**, *33*, 1360–1367.

(33) LePage, W. S.; Chen, Y.; Kazyak, E.; Chen, K.-H.; Sanchez, A. J.; Poli, A.; Arruda, E. M.; Thouless, M. D.; Dasgupta, N. P. Lithium Mechanics: Roles of Strain Rate and Temperature and Implications for Lithium Metal Batteries. *J. Electrochem. Soc.* **2019**, *166* (2), A89–A97.